

1 **Congenital disorder of glycosylation caused by starting site-specific variant in syntaxin-5**

2

3 Peter T.A. Linders<sup>1</sup>, Eveline C.F. Gerretsen<sup>1</sup>, Angel Ashikov<sup>2,3</sup>, Mari-Anne Vals<sup>4,5</sup>, Natalia H. Revelo<sup>1</sup>, Richard  
4 Arts<sup>1</sup>, Melissa Baerenfaenger<sup>2</sup>, Fokje Zijlstra<sup>3</sup>, Karin Huijben<sup>3</sup>, Kimiyo Raymond<sup>6</sup>, Kai Muru<sup>5,7</sup>, Olga Fjodorova<sup>7</sup>,  
5 Sander Pajusalu<sup>5,7</sup>, Katrin Õunap<sup>5,7</sup>, Martin ter Beest<sup>1</sup>, Dirk Lefeber<sup>2,3,\*</sup> and Geert van den Bogaart<sup>1,8,\*</sup>

6

7 <sup>1</sup> Department of Tumor Immunology, Radboud University Medical Center, 6525 GA Nijmegen, The Netherlands

8 <sup>2</sup> Department of Neurology, Donders Institute for Brain, Cognition and Behavior, Radboud University Medical  
9 Center, 6525 GA, Nijmegen, The Netherlands

10 <sup>3</sup> Translational Metabolic Laboratory, Department of Laboratory Medicine, Radboud University Medical  
11 Center, 6525 GA, Nijmegen, The Netherlands

12 <sup>4</sup> Children's Clinic, Tartu University Hospital, Estonia

13 <sup>5</sup> Department of Clinical Genetics, Institute of Clinical Medicine, University of Tartu, Estonia

14 <sup>6</sup> Department of Laboratory Medicine and Pathology, Mayo College of Medicine, Rochester, Minnesota, USA.

15 <sup>7</sup> Department of Clinical Genetics, United Laboratories, Tartu University Hospital, Tartu, Estonia

16 <sup>8</sup> Department of Molecular Immunology, Groningen Biomolecular Sciences and Biotechnology Institute,  
17 University of Groningen, 9747AG, Groningen, Netherlands

18 \* Correspondence: [dirk.lefeber@radboudumc.nl](mailto:dirk.lefeber@radboudumc.nl); Tel.: +31-24-36-14567; [g.van.den.bogaart@rug.nl](mailto:g.van.den.bogaart@rug.nl); Tel.: +31-  
19 50-36-35230

20

21 **Abstract**

22 The SNARE (soluble N-ethylmaleimide-sensitive factor attachment protein receptor) protein syntaxin-5 (Stx5)  
23 is essential for Golgi transport. In humans, the *STX5* mRNA encodes two protein isoforms, Stx5 Long (Stx5L)  
24 from the first starting methionine and Stx5 Short (Stx5S) from an alternative starting methionine at position  
25 55. In this study, we identified a novel human disorder caused by a single missense substitution in the second  
26 starting methionine (p.M55V), resulting in complete loss of the short isoform. Patients suffer from an early  
27 fatal multisystem disease, including severe liver disease, skeletal abnormalities and abnormal glycosylation.

28 Whereas Golgi morphology was unaltered, primary human dermal fibroblasts isolated from these patients

29 **NOTE: This preprint reports new research that has not been certified by peer review and should not be used to guide clinical practice.**  
showed defective glycosylation and mislocalization of glycosyltransferases. Measurements of anterograde

30 trafficking, based on biotin-synchronizable forms of Stx5 (the RUSH system), and of cognate binding SNAREs,  
31 based on Förster resonance energy transfer (FRET), revealed that the short isoform of Stx5 is essential for  
32 intra-Golgi transport. This is the first time a mutation in an alternative starting codon is linked to human  
33 disease, demonstrating that the site of translation initiation is an important new layer of regulating protein  
34 trafficking.

35 **Keywords**

36 Syntaxin-5, ER-Golgi trafficking, glycosylation, secretory pathway, congenital disorders of glycosylation

37

## 38 Introduction

39 In eukaryotes, proteins destined for the secretory pathway are synthesized at the endoplasmic reticulum (ER)  
40 and then transported to the Golgi apparatus, where they are sorted for their ultimate destinations at the  
41 *trans*-Golgi network. Central to this process is intracellular membrane fusion, which is mediated by members  
42 of the SNARE (soluble *N*-ethylmaleimide-sensitive factor attachment protein receptor) protein family.  
43 Membrane fusion is the result of the formation of a tight alpha-helical coiled-coil bundle by cognate SNARE  
44 proteins that are present in both the carrier vesicle and target membranes. Membrane fusion requires an R-  
45 SNARE, characterized by an arginine residue located central in the SNARE bundle, and three Q-SNAREs, with  
46 glutamine residues instead. For anterograde ER to Golgi trafficking, the target (t-) SNARE complex is formed by  
47 the Qa-SNARE syntaxin-5 (Stx5)<sup>1-4</sup>, together with the Qb-SNAREs GosR1 (also known as GS27 or membrin) or  
48 GosR2 (GS28), and R-SNAREs Ykt6 or Sec22b (Ers24)<sup>5-7</sup>. Generally in mammalian cells, the R-SNAREs act as  
49 vesicle (v-) SNAREs and the Q-SNAREs together form the t-SNARE complex on the target membrane<sup>8</sup>. In  
50 contrast, the Qc-SNAREs Bet1 and Bet1L (GS15) function as the v-SNAREs at the ER/Golgi interface<sup>9-12</sup>. This  
51 possibly prevents the formation of non-functional SNARE complexes during ER to Golgi transit. In addition,  
52 Stx5 functions in retrograde intra-Golgi transport by forming a SNARE complex with GosR1, Bet1L, and Ykt6<sup>12,13</sup>  
53 and in retrograde trafficking from endosomes to the *trans*-Golgi network (TGN)<sup>14,15</sup>, making it a unique SNARE  
54 protein involved in both anterograde and retrograde Golgi transport.  
55 *STX5* is highly conserved and is an essential gene in animals and fungi<sup>16,17</sup>. In animals, Stx5 exists as a long and  
56 a short isoform translated from the same mRNA: 39.6 kDa sized Stx5 Long (Stx5L) and 34.1 kDa sized Stx5  
57 Short (Stx5S)<sup>13,18</sup>. This is in contrast to lower organisms such as *Saccharomyces cerevisiae*, which only  
58 expresses a single isoform of Stx5 (Sed5p), likely resembling mammalian Stx5L with the presence of an N-  
59 terminal COPI-binding tribasic motif<sup>19</sup>. The emergence of a second Stx5 isoform can be traced back to the  
60 pacific purple sea urchin, *Strongylocentrotus purpuratus*, and is also present in the model organism *Danio*  
61 *rerio*, but not in *Drosophila melanogaster* or *Caenorhabditis elegans*. Compared to Stx5S, Stx5L contains 54  
62 extra N-terminal residues bearing an Arginine – Lysine – Arginine (RKR) ER retrieval motif, and as a result, Stx5L  
63 locates more to the ER whereas Stx5S locates more to the Golgi network<sup>13,18,20-22</sup>. The evolutionary necessity of  
64 Stx5L remains unclear but it has been suggested that Stx5L is important to maintain ER structure by binding  
65 microtubules, possibly via CLIMP-63<sup>21,23</sup>. In addition, immunoprecipitations showed that GosR1 and Bet1L  
66 preferentially interact with Stx5S over Stx5L<sup>24,25</sup>, suggesting that Stx5S might act in more fusogenic complexes

67 later at the ER-Golgi interface whereas Stx5L might be more involved in earlier fusion steps. In the present  
68 study, we identified a genetic variant in the second translation codon methionine-55, fully abrogating the  
69 production of Stx5S and providing a unique opportunity to study the physiological relevance of the existence  
70 of two isoforms in humans. Patients homozygous for this mutation have a very severe clinical phenotype  
71 associated with infantile mortality and defective protein glycosylation. We demonstrate that although Stx5L  
72 can largely compensate for the lack of Stx5S, the loss of Stx5S leads to defects in anterograde Golgi trafficking  
73 with mislocalization of glycosyltransferases, which results in pronounced defects in glycosylation. Moreover,  
74 by synchronizing the intracellular trafficking of Stx5 isoforms, we reveal differential trafficking routes for either  
75 isoform and identify Stx5S as the dominant Qa-SNARE for intra-Golgi transport. This is the first time that a  
76 mutation in an alternate starting site of ribosomal translation is related to human disease. This finding reveals  
77 that protein function can be regulated at the level of translation initiation and has profound effects on  
78 intracellular membrane trafficking and Golgi function.

79

## 80 **Results**

### 81 *Clinical data*

82 The family history ([Supplementary Figure 1](#)) revealed multiple deceased individuals (IV:3, IV:9, IV:10) shortly  
83 after birth, spontaneous abortions (IV:5, IV:6, IV:7), and elective abortions in the 20th-21st week of pregnancy  
84 due to abnormal fetal ultrasound (US) (IV:4, IV:8). Fetal US of individuals IV:8, IV:9, and IV:10 ([Figure 1a-c](#),  
85 [respectively](#)) showed shortening of the long bones with suspicion of chondrodysplasia. Patients IV:9 and IV:10  
86 showed highly dysmorphic facial features (high forehead, frontal bossing, prominent glabella, short and  
87 upturned nose, long philtrum, micrognathia and dysplastic ears), skeletal dysplasia (short extremities and  
88 narrow thorax), profound hypotonia, hepatomegaly, and many abnormal laboratory parameters including  
89 elevated cholesterol ([Figure 1b, c](#), [Supplementary Table 1](#)). After birth, the main clinical problem for both  
90 patients IV:9 and IV:10 was progressive liver failure with cholestasis and hyperinsulinemic hypoglycemia  
91 ([Supplementary Table 1](#)). Liver failure was the main cause of death at the age of 28 days and 8 months, in  
92 patients IV:9 and IV:10, respectively. Autopsy of fetus IV:8 revealed bilateral hydronephrosis and sacral  
93 lordosis. Autopsy of patient IV:9 showed hepatomegaly with stage 3 to 4 liver fibrosis, agenesis of left kidney,  
94 hyperemia of internal organs, ventricular septal defect and suggestive pathohistological features of

95 chondrodysplasia. Autopsy of patient IV:10 showed biliary cirrhosis and nodular regenerative hyperplasia,  
96 pancreatic hypertrophia/hyperplasia, and narrow thorax with normal lung development.

97

### 98 ***Abnormal protein glycosylation suggests a defect in Golgi trafficking***

99 Known genetic causes for skeletal dysplasias were excluded (IV:8), no submicroscopic chromosomal  
100 abnormalities were found, while most metabolic investigations were normal except for the Congenital  
101 Disorders of Glycosylation (CDG) (IV:9 and IV:10). CDG screening revealed a strong hyposialylation of protein  
102 N-glycosylation and mucin-type O-glycosylation, as analyzed by isofocusing of respectively plasma transferrin  
103 (Fig 1d) and apolipoprotein CIII (ApoCIII-IEF, Fig 1e). ApoCIII-IEF showed a strong increase of non-sialylated  
104 apoCIII (ApoCIII-0), even stronger than observed for genetic defects in the Conserved Oligomeric Golgi (COG)  
105 complex, a known group of disorders with disturbed Golgi homeostasis and abnormal glycosylation. To gain  
106 more insight into the abnormal N-glycan structures, mass spectrometry was performed of intact transferrin  
107 (Fig 1f, g, Supplementary Figure 2) and of total plasma protein derived N-glycans (Fig 1f, h, Supplementary  
108 Figure 3). Analysis of intact transferrin of individuals IV:9 and IV:10 revealed multiple abnormal glycan  
109 structures, divided into two categories: high mannose structures and truncated glycans. A dominant  
110 accumulation was found of high-mannose glycans (Supplementary Table 2, Man5, mass/peak number)  
111 suggesting a problem with MGAT1, the enzyme that adds the next *N*-acetylglucosamine during N-  
112 glycosylation. Furthermore, a series of transferrin isoforms was observed with reduced incorporation of  
113 galactose and sialic acid residues. Analysis of N-glycans released from total plasma proteins recapitulated the  
114 two categories of abnormal glycans with the accumulation of high mannose glycans, as well as reduced  
115 incorporation of galactose and sialic acid residues (Supplementary Table 3).  
116 Together, these data indicate that the activities of multiple glycosyltransferases in the Golgi apparatus are  
117 affected, covering both N- and O-glycosylation, thereby suggesting a general disturbance in Golgi trafficking.

118

### 119 ***Molecular investigations result in the identification of variants in STX5***

120 Chromosomal microarray analysis (CMA) using HumanCytoSNP-12 microarrays revealed multiple long  
121 contiguous stretches of homozygosity (LCSH, >5 Mb) distributed across the entire genome, with several  
122 regions of homozygosity on chromosome 11 in all three affected sibs (IV:8, IV:9 and IV:10, Supplementary  
123 Table 4). Exome sequencing was performed in proband IV:9 to find the genetic variant that could be associated

124 with the disease. Only two homozygous rare protein-altering variants without homozygous individuals in the  
125 gnomAD v3 database were identified in shared homozygous stretches on chromosome 11. First, a missense  
126 variant in the *VPS37C* gene was discovered (NM\_017966.4:c.760G>T p.(Gly254Cys) rs201088253). However, as  
127 this variant reaches an allele frequency of 0.9% in Estonia, it is unlikely to cause a rare genetic disorder. The  
128 second variant was identified in the *STX5* gene (NM\_003164.4:c.163A>G p.(Met55Val), Fig 2a). This is a  
129 missense mutation affecting the alternative starting codon for the production of the short Stx5 isoform. The  
130 variant is absent from the gnomAD v3 database and was thus classified as a potentially disease-causing  
131 variant. The variant was confirmed by Sanger sequencing as homozygous in all affected individuals (IV:8, IV:9,  
132 and IV:10) and as heterozygous in the mother (III:2). Paternal DNA was not available for testing.  
133 To confirm the effect of the genetic variant on both Stx5 proteoforms, immunoblotting was performed in  
134 primary dermal fibroblasts of patients IV:9 and IV:10. While Stx5L was present, a total absence of Stx5S was  
135 found in both patient fibroblasts (Fig. 2b, c). We next tested the expression of known interaction partners of  
136 Stx5. The levels of Qc-SNARE Bet1L (Fig. 2b, c), which forms a complex with Stx5 upon retrograde intra-Golgi  
137 trafficking<sup>12-15</sup>, were also reduced. In contrast, the expression of Qc-SNARE Bet1, which forms a complex with  
138 Stx5 upon anterograde ER-Golgi trafficking<sup>5,7,13,26</sup> was not reduced (Fig. 2b, c). Likewise, the expression of Qb-  
139 SNAREs GosR1 and GosR2, which can complex with Stx5 for anterograde ER-Golgi trafficking and retrograde  
140 intra-Golgi trafficking<sup>4,5,7,12,13,24</sup> were unaltered in patient dermal fibroblast lysates. We hypothesized that a  
141 compensatory mechanism might exist by upregulating the expression of the *trans*-Golgi Qa-SNARE Stx16<sup>27</sup>,  
142 usually involved in endosome-to-TGN trafficking<sup>28</sup>, but we did not detect a change of Stx16 expression in  
143 patient fibroblast lysates (Fig. 2b, c). As a first step to confirm that fibroblasts offer a useful model to  
144 recapitulate the cell biological abnormalities due to loss of the Stx5S isoform, we studied glycosylation by  
145 fluorescently-labeled lectins.

146

#### 147 ***Glycosylation defects in Stx5M55V patient fibroblasts***

148 Cell surface staining with the lectin SNA-I from *Sambucus nigra*, which binds terminal sialic acid in an  $\alpha$ -2,6  
149 linkage of fully-formed N-glycan moieties and, to a lesser extent, sialic acid in an  $\alpha$ -2,3 linkage, showed that  
150 glycosylation was also impaired at the cellular level in patient fibroblasts. Compared to fibroblasts of healthy  
151 donors, we observed a more than two-fold reduced SNA-I labeling intensity in Stx5M55V patient fibroblasts  
152 (Fig. 2d,e). To confirm this glycosylation defect, we performed cell surface staining with the lectin PNA (Peanut

153 agglutinin) from *Arachis hypogaea*, which binds terminal galactose residues present on mucin O-glycan  
154 moieties. Opposite to our findings with SNA-I, we observed an increased labeling intensity in Stx5M55V patient  
155 fibroblasts relative to healthy control by about eight-fold (Fig. 2f,g). As these results reiterate the glycosylation  
156 defect observed on serum transferrin, total plasma N-glycans and apoCIII mucin O-glycans, using patient  
157 fibroblasts is a suitable model to investigate the cell biological consequences of the complete disruption of the  
158 Stx5S isoform.

159

### 160 ***Stx5M55V mutation results in mislocalization of glycosyltransferases***

161 Given that Stx5 mediates ER-Golgi trafficking<sup>2,4-7,12,13,15,24,26</sup>, we next investigated whether the glycosylation  
162 defect in Stx5M55V patient fibroblasts was caused by the mislocalization of glycosyltransferases. We  
163 performed immunofluorescence labeling of mannosyl ( $\alpha$ -1,3-)-glycoprotein  $\beta$ -1,2-N-  
164 acetylglucosaminyltransferase (MGAT1, also known as GnTI), which catalyzes the addition of GlcNAc to the  
165 immature man-5 N-glycan. Compared to healthy donor fibroblasts, MGAT1 colocalizes only slightly less with  
166 the *cis*-Golgi marker GM130 in patient fibroblasts (Supplementary Fig. 4a, b), but colocalized substantially less  
167 with the *trans*-Golgi network marker TGN46 (Fig. 3a, b). In contrast, alpha-mannosidase 2 (MAN2A1), which  
168 catalyzes the final hydrolytic step in the N-glycan maturation pathway after MGAT1 conversion, colocalized  
169 substantially less with both GM130 (Fig. 3c, d) and TGN46 (Supplementary Fig. 4c, d). Similarly to MGAT1,  
170 beta-galactoside alpha-2,6-sialyltransferase 1 (ST6GAL1), which catalyzes the transfer of sialic acid to galactose  
171 residues of N-glycans in an  $\alpha$ -2,6 linkage, colocalized less with both GM130 (Supplementary Fig. 4e, f) and  
172 TGN46 (Supplementary Fig. 4g, h). Finally, N-acetylgalactosaminyltransferase 2 (GALNT2), which catalyzes the  
173 initial reaction in mucin O-linked glycan synthesis, localized more to the *cis*-Golgi (marker Zinc finger protein-  
174 like 1 (ZFPL1)<sup>29</sup>) (Fig. 3e, f) and less to the *trans*-Golgi (Fig. 3g, h).

175 Taken together, the loss of Stx5S results in irregular localization of glycosyltransferases to the Golgi apparatus.  
176 Mislocalization of glycosyltransferases can have a profound impact on glycosylation as shown by  
177 computational simulations<sup>30</sup>. Notwithstanding these large defects in glycosylation in the Stx5M55V patients,  
178 negative staining electron microscopy and immunofluorescence labeling of *cis*- and *trans*-Golgi markers  
179 showed no large alterations in Golgi morphology and the polarized arrangement of Golgi apparatus cisternae  
180 was still present in Stx5M55V fibroblasts (Supplementary Figure 5). These results indicate that although Stx5L

181 is sufficient to maintain normal Golgi apparatus morphology, Stx5S is required for proper trafficking of  
182 glycosylation enzymes.

183

#### 184 ***Stx5 mediates retrograde Golgi trafficking***

185 As Stx5 is required for trafficking of glycosylation enzymes, we then studied the role of the two Stx5 isoforms  
186 in ER-Golgi trafficking. Because Stx5L contains an RKR ER-retrieval motif in its N-terminal extension, it locates  
187 more at the ER compared to Stx5S<sup>13,18,20,21</sup>. In line with this, we observed a more dominant localization of Stx5L  
188 at the ER and less at various Golgi compartments in Stx5M55V fibroblasts compared to total Stx5 localization  
189 in healthy control fibroblasts (Fig. 4a, b, d, e, Supplementary Fig. 6a, b, d, e). A notable difference was the far  
190 more diffuse staining in Stx5M55V patients of the COPI coat protein  $\beta$ COP (Fig. 4a, c) and of TGN46 (Fig. 4d, f).  
191 In contrast, we observed a small increase in GM130 fluorescence in Stx5M55V patients (Supplementary Fig.  
192 6f). Western blot showed that total cellular levels of  $\beta$ COP and GM130 were not altered in Stx5M55V patients  
193 (Fig. 4g). In contrast, total TGN46 protein levels were reduced in patient fibroblasts (Fig. 4h). These findings  
194 suggest that loss of Stx5S results in reduced COPI trafficking between GM130-marked *cis*- and TGN46-marked  
195 *trans*-Golgi compartments. As COPI is also involved in retrograde Golgi-ER transport<sup>31</sup>, we investigated  
196 whether trafficking at this interface is compromised in Stx5M55V fibroblasts by using the fungal metabolite  
197 Brefeldin A (BFA), which inhibits COPI vesicle formation<sup>32</sup>. If loss of Stx5S results in reduced retrograde Golgi-  
198 ER transport, we expect reduced relocalization of Golgi-resident proteins to ER upon BFA treatment. Indeed,  
199 redistribution of GALNT2 from the Golgi to the ER was incomplete in patient fibroblasts (Fig. 5a, b), showing a  
200 role for Stx5S in retrograde COPI trafficking. To delineate the role of Stx5L in this process, we generated two  
201 clonal HeLa cell lines lacking Stx5L by CRISPR/Cas9 (Stx5 $\Delta$ L: B1A7 and C1F4). In these cells, BFA resulted in  
202 faster relocalization of GALNT2 to the ER compared to parental HeLa (Fig. 5c, d), indicating that Stx5S suffices  
203 for retrograde COPI trafficking and the expression of Stx5L is rate-limiting for this process. Further  
204 investigation of anterograde trafficking in Stx5 $\Delta$ L cells with H-89 washout (Supplementary fig. 7a, b), the RUSH  
205 system for synchronized ER-Golgi transport<sup>33</sup> (Supplementary fig. 7c, d, Supplementary movies 1, 2) and  
206 temperature-synchronizable VSVG<sup>34</sup> (Supplementary fig. 7e, f, Supplementary movies 3, 4) revealed no  
207 phenotype relating to the loss of Stx5L. Thus, these data suggest Stx5L has no necessary function in ER-Golgi  
208 trafficking as Stx5S can compensate, while Stx5L can only partly compensate for the loss of Stx5S.

#### 209 ***Discerning the roles of Stx5 isoforms in ER and Golgi trafficking***



210 Our results in patient fibroblasts indicate a differential trafficking role of the two Stx5 isoforms in anterograde  
211 ER to Golgi trafficking. To gain more insight in this process, we fused each Stx5 isoform to streptavidin-binding  
212 protein (SBP) and mCitrine (Stx5L-SBP-mCitrine and Stx5S-SBP-mCitrine). Moreover, we generated a mutant  
213 form of Stx5L where the RKR ER-retrieval motif was converted to 3x alanine (AAA) (Stx5L $\Delta$ ER-SBP-mCitrine)<sup>18</sup>,  
214 to delineate the role of this motif in ER-Golgi transport. The co-expression of these constructs with ER-  
215 localized streptavidin enabled the synchronized release of the Stx5 fusion proteins from the ER using biotin,  
216 which is the so-called RUSH system<sup>33</sup> (Fig. 6a). Co-expressing each Stx5 isoform with the Golgi marker Giantin  
217 fused to mScarlet<sup>35</sup> in wildtype HeLa cells, allowed to visualize the trafficking of Stx5-SBP-mCitrine to the Golgi  
218 following the addition of biotin (Fig. 6a, b, Supplementary movies 5-7). All three Stx5 isoforms reached the  
219 Golgi with the same rate and achieved maximal Golgi localization after 20 minutes (Fig. 6c). However, the  
220 subsequent decrease in Golgi localization, attributed to recycling to the ER or probable degradation of the  
221 fusion proteins, was faster for Stx5L-SBP-mCitrine than for than for Stx5S or Stx5L $\Delta$ ER (Fig. 6c). Thus, the RKR  
222 ER retrieval motif of Stx5L is necessary and sufficient for the attenuated presence of Stx5L at the Golgi,  
223 supporting that the main role of Stx5S is COPI trafficking specifically at the Golgi.

224

### 225 ***The two isoforms of Stx5 differently engage in SNARE complexes***

226 Since interactions of Stx5 with Bet1 and Bet1L mediate anterograde ER-Golgi transport and retrograde intra-  
227 Golgi transport, respectively<sup>9-12</sup>, we hypothesized that Stx5S would interact more strongly with Bet1L, whereas  
228 Stx5L would interact more strongly with Bet1. We set out to test this hypothesis by performing co-  
229 immunoprecipitation with our RUSH Stx5 constructs. However, we were unable to resolve differences in  
230 binding to endogenous cognate Qc-SNAREs between the two Stx5 isoforms, either without or with 30 mins  
231 biotin (Supplementary Fig. 8a, b). A likely explanation is that interactions might occur *in vitro* during the  
232 immunoprecipitation. Therefore, we developed an approach to visualize SNARE complexes based on a  
233 combination of the RUSH system<sup>33</sup> and our previously developed Förster resonance energy transfer-  
234 fluorescence lifetime imaging microscopy (FRET-FLIM) approach for visualization of SNARE complexes<sup>36</sup> (Fig.  
235 7a). The FRET-FLIM approach employed Stx5 isoforms C-terminally fused with a donor fluorophore (mCitrine)  
236 and Bet1L C-terminally fused with an acceptor fluorophore (mCherry). The formation of a post-fusion SNARE  
237 complex results in the close proximity of the donor and an acceptor fluorophore resulting in FRET which can be  
238 measured from a decreased donor fluorescence lifetime ( $\tau$ ). Contrary to ratiometric FRET, FRET-FLIM is not

239 dependent on local concentration differences or excitation intensities of the donor and acceptor fluorophores,  
240 as  $\tau$  is an intrinsic property of the fluorophore itself. By combining the FRET-FLIM approach with the RUSH  
241 system, we were able to control the spatial localization of Stx5 isoforms and measure interactions specifically  
242 at the ER (no biotin) or the Golgi apparatus (20 min after biotin addition). 30 minutes prior to imaging, cells  
243 were incubated with cycloheximide in culture medium to make sure background interaction from any ER-  
244 localized newly synthesized acceptor construct was mitigated.

245 For the mCitrine donor-only Stx5 constructs, we measured similar lifetimes for both isoforms (Fig. 7c,  
246 Supplementary Fig. 9a, Stx5L: 3.02 ns  $\pm$  0.004, Stx5S: 2.99 ns  $\pm$  0.007) prior to biotin addition, while these  
247 lifetimes slightly decreased following biotin addition (Fig. 9d, Supplementary Fig. 9a, Stx5L: 2.90 ns  $\pm$  0.006,  
248 Stx5S: 2.86 ns  $\pm$  0.011). We attribute this reduced lifetime to the fact that mCitrine is somewhat pH-sensitive<sup>37</sup>  
249 and the pH of the Golgi apparatus is lower than in the ER lumen<sup>38</sup>. We then co-expressed the Stx5 isoforms  
250 with mCherry-tagged Bet1L (Bet1L-mCherry) (Fig. 7a,b). At the ER, thus before the release of Stx5 with biotin,  
251 we observed reduced lifetimes for both Stx5S and Stx5L with Bet1L-mCherry, compared to the donor-only  
252 controls (Fig. 7b, c, Supplementary fig. 9b, Stx5L: 2.82 ns  $\pm$  0.01, Stx5S: 2.79  $\pm$  0.01), whereas the lifetimes of  
253 Stx5S and Stx5L did not significantly differ from each other. After the release in the presence of biotin, this  
254 difference between Stx5L and Stx5S became significant and lifetimes were 2.63 ns ( $\pm$  0.01) for Stx5L while  
255 Stx5S dropped to 2.52 ns ( $\pm$  0.03) (Fig. 7b, d, Supplementary fig. 9c). To validate that the observed effect is  
256 indeed caused by functional SNARE complex formation, we repeated this experiment with VAMP8 instead of  
257 Bet1L as the acceptor R-SNARE. VAMP8 has no role in ER-Golgi membrane fusion but rather associates with  
258 the late endosomal/lysosomal compartment<sup>28,36,39-43</sup>. We only observed minor decreases in fluorescence  
259 lifetimes for both Stx5L and Stx5S (Supplementary fig. 9d, e, g, prior to biotin Stx5L: 2.92 ns  $\pm$  0.01, Stx5S: 2.86  
260  $\pm$  0.02, upon biotin addition Supplementary fig. 9d, f, h, Stx5L: 2.82 ns  $\pm$  0.01, Stx5S: 2.76  $\pm$  0.02). The FLIM  
261 results with VAMP8 demonstrate that Stx5S interacts more strongly with Bet1L at the Golgi than Stx5L. Thus,  
262 Stx5S is the dominant Qa-SNARE for intra-Golgi trafficking.

263

## 264 Discussion

265 Since the advent of the genomic age, close to 6000 monogenic disorders have been discovered<sup>44</sup>. While nearly  
266 all of these disorders result in a truncated, unstable and/or nonfunctional protein, e.g. due to a genetic variant  
267 in the catalytic site or protein misfolding, isoform-specific mutations are rare. Here we present the first known

268 mutation in an alternate site of ribosomal translation leading to human disease, namely the mutation of the  
269 second starting methionine of Stx5. This mutation leads to the complete and specific loss of Stx5S. Although  
270 STX5 is an essential gene for embryonic development in mice<sup>16,17</sup>, here we show that in humans the loss of  
271 Stx5S still allowed a completed pregnancy. Nevertheless, patients have a very severe clinical pathology  
272 characterized by infantile mortality due to liver disease, skeletal abnormalities and protein glycosylation  
273 defects. While the exact mechanism for alternative translation is unclear, this might be an actively regulated  
274 process. It could also be simply regulated by the affinity of the ribosome for the nucleotide sequence upstream  
275 of the starting codon. Supporting the latter option, analysis of translation initiation sites with NetStart<sup>45</sup>  
276 revealed that the starting codon of Stx5S is located in a more optimal nucleotide context than the starting  
277 codon for Stx5L (Supplementary fig. 10). This could lead to more leaky ribosomal scanning<sup>46,47</sup>, resulting in a  
278 lower expression of Stx5L than Stx5S in controls.

279 Cofractionation and microscopy studies have revealed that the localization of Stx5L and Stx5S overlap to a  
280 large extent, but that they are generally distributed as a gradient between ER, ERGIC, and Golgi apparatus<sup>20</sup>.  
281 This observation has previously led to the suggestion that Stx5L might play a role in early Golgi trafficking,  
282 while Stx5S functions in late Golgi trafficking<sup>2,4-7,12,13,15,24,26</sup>. Our data now shows that this is not the case and  
283 that both Stx5 isoforms can mediate both early and late anterograde and retrograde trafficking with sufficient  
284 fidelity to keep the layered Golgi morphology intact. However, the role of Stx5S is more important for  
285 anterograde trafficking, and its absence leads to an altered Golgi distribution of glycosylation enzymes and  
286 trafficking proteins. In contrast, loss of Stx5L leads to faster anterograde trafficking suggesting it might be  
287 more involved in retrograde trafficking and/or sequestering interactions partners of Stx5S. The dominant role  
288 of Stx5S in intra-Golgi trafficking is corroborated by the observation that cellular levels of Bet1L, with known  
289 roles in intra-Golgi trafficking, are lower in Stx5M55V patient cells. Interestingly, genetic variants in conserved  
290 oligomeric Golgi (COG) tethering complex components, which are also implicated in CDGs, resulted in lower  
291 levels of Bet1L as well<sup>48</sup>. Although the Stx5-Bet1L interaction has been reported in several studies<sup>14,31</sup>, our  
292 study now shows this interaction *in situ* using FLIM. This interaction is localization dependent and occurs  
293 mostly when Stx5 is localized at the Golgi. Moreover, we observed stronger interaction of Bet1L with Stx5S  
294 compared to Stx5L at the Golgi, which is likely the result of the differential localization of both isoforms.

295 An important function of the Golgi apparatus is protein glycosylation<sup>49</sup>. Collectively, somatic mutations  
296 affecting glycosylation are classified as CDGs and currently over 100 monogenic diseases affecting

297 glycosylation have been identified<sup>50,51</sup>. A significant number of these include defects in Golgi trafficking, such  
298 as the components of the conserved oligomeric Golgi tethering complex (COG)<sup>52-60</sup>, mutations in genes coding  
299 for the vacuolar H<sup>+</sup>-ATPase and its assembly factors<sup>61-64</sup>, and novel genes involved in Golgi ion homeostasis<sup>65-</sup>  
300 <sup>67</sup>. Furthermore, defects are known in components associated with COPI-coated vesicles<sup>68</sup> that result in  
301 deficient protein glycosylation in patient cells, but are not linked to abnormal glycosylation of proteins in  
302 plasma and thus escape routine CDG screening. Our study is the first example of an ER-Golgi SNARE being  
303 implicated in CDG, thus highlighting the potential of glycosylation screening in patients to uncover novel cell  
304 biological mechanisms.

305 While the cellular effects of the loss of Stx5S in Stx5M55V mutant fibroblasts are subtle, there can be  
306 pronounced consequences in secretory cells, such as exocrine and endocrine cells, which are sensitive to  
307 minor disruptions of the secretory pathway<sup>49,68-70</sup>. Recent modeling showed that the slight mislocalization of  
308 glycosyltransferases can result in large differences in glycosylation patterns, because glycosylation is the result  
309 of the sequential addition and removal of different sugar moieties at the various Golgi compartments<sup>30</sup>. The  
310 defects in intra-Golgi trafficking can explain the other pathologies as well. For instance, Stx5 can participate in  
311 the trafficking and processing of the very low-density lipoprotein receptor (VLDL-R) and this role is heavily  
312 dependent on the expression of Stx5<sup>71</sup>, thus providing an explanation for the observed cholesterol  
313 homeostasis defect with elevated cholesterol in all Stx5M55V patients.

314 In summary, we have demonstrated the first known mutation in an alternative starting codon leading to  
315 human disease, with severe impact on intracellular membrane trafficking and leading to the discovery of a  
316 novel CDG.

317

### 318 **Acknowledgments**

319 We thank the family for participating in this study. We thank following people for constructs: Hesso Farhan  
320 and Franck Perez (Str-KDEL\_ManII-SBP-EGFP; Addgene plasmid #65252), Jennifer Lippincott-Schwartz (pEGFP-  
321 VSVG; Addgene plasmid #11912) and Feng Zhang (pSpCas9n(BB)-2A-Puro (PX462) V2.0; Addgene plasmid  
322 #62987). We also thank the Microscopic Imaging Center of the Radboud Institute for Molecular Life Sciences  
323 for use of their microscopy facilities. N.H.R. is funded by a Long-Term Fellowship from the European Molecular  
324 Biology Organization (EMBO-LTF, ALTF 232-2016) and a Veni grant from the Netherlands Organization for  
325 Scientific Research (016.VENI.171.097). G.v.d.B. is funded by a Young Investigator Grant from the Human

326 Frontier Science Program (HFSP; RGY0080/2018) and a Vidi grant from the Netherlands Organisation for  
327 Scientific Research (NWO-ALW VIDI 864.14.001). D.J.L. is funded by a Vidi grant (ZONMW VIDI 917.13.359), a  
328 ZONMW Medium Investment Grant (40-00506-98-9001) from the Netherlands Organisation for Scientific  
329 Research, and Erare grants EUROCDG2 and Euroglycanomics. K.Õ, M.-A.V., S.P., and K.M. were supported by  
330 the Estonian Research Council grants GARLA8175, PUT355, PUTJD827 and PRG471.

331

### 332 **Author Contributions**

333 P.T.A.L., M.t.B., D.J.L., and G.v.d.B. designed the experiments and wrote the paper. E.C.F.G. contributed to the  
334 Stx5 kinetics, co-immunoprecipitation, and FLIM experiments. A.A., M.-A.V., M.B., F.Z., K.H., K.R., K.M., and  
335 K.Õ. contributed to the clinical data, exome sequencing and glycomics. O.F. and S.P. performed homozygosity  
336 mapping and prioritization of exome variants. N.H.R. performed TEM. R.A. contributed to the Stx5ΔL  
337 experiments. P.T.A.L. and M.t.B. performed all other experiments. All authors contributed to writing the  
338 manuscript.

339

### 340 **Declaration of Interests**

341 The authors declare that they have no competing financial interests.

342

### 343 **Methods**

#### 344 *Ethics*

345 The study was approved by Research Ethics Committee of the University of Tartu (approval dates 19.12.2011,  
346 20.02.2012 and 17.03.2014, and approval numbers 210/M-17, 212/M-31 and 235/M-13, 17.03.2014,  
347 respectively) and were strictly in accordance with the Declaration of Helsinki. Informed consent for carrying  
348 out research was obtained from the family of investigated individuals.

349

#### 350 *Glycosylation studies*

351 Screening for Congenital Disorders of Glycosylation (CDG) was carried out as described before<sup>62</sup>. Plasma N-  
352 glycan profiling was performed by MALDI-TOF mass spectrometry of permethylated glycans<sup>72</sup>, using 10 μL of  
353 plasma. High resolution mass spectrometry of intact transferrin was performed on a 6540 nanochip QTOF  
354 (Agilent), according to published protocols<sup>73</sup>.

355

356 *Microarray analysis*

357 DNA was extracted either from peripheral blood according to the standard salting out protocol (IV:9 and IV-  
358 :10) or from amniotic fluid cell culture (IV:8). Screening for chromosomal abnormalities was performed using  
359 HumanCytoSNP-12 BeadChips (Illumina Inc., San Diego, CA, USA). 200 ng of total DNA per sample was  
360 processed according to the protocol supplied by the manufacturer. Genotypes were called by GenomeStudio  
361 v2011.1 software and the data were analyzed using GenomeStudio Genome Viewer tool (Illumina Inc.). The  
362 minimum threshold for LCSH (long contiguous stretches of homozygosity) regions was set at 5 Mb.

363

364 *Exome sequencing*

365 Genomic DNA was extracted from fibroblasts from patient IV:9 according to the manufacturer's protocol using  
366 a Qiagen Mini Kit (Qiagen) and was checked for DNA degradation on agarose gels. Next generation sequencing  
367 (NGS) and analysis was performed as described<sup>63</sup>. In brief, exome enrichment was performed using the  
368 SureSelect Human All Exon 50 Mb Kit (Agilent), covering ~21,000 genes. The exome library was sequenced on a  
369 SOLiD 5500xl sequencer (Life Technologies). Color space reads were iteratively mapped to the hg19 reference  
370 genome with the SOLiD LifeScope software version 2.1. Called variants and indels were annotated using an in-  
371 house annotation pipeline<sup>74,75</sup> and common variants were filtered out based on a frequency of >0.5 % in  
372 dbSNP and a frequency of >0.3 % in our in-house database of >5,000 exomes. Quality criteria were applied to  
373 filter out variants with less than 5 variant reads and less than 20 % variation. Furthermore, synonymous  
374 variants, deep intronic, intergenic and UTR variants were excluded. The identified variant was confirmed by  
375 Sanger sequencing in all affected individuals (IV:8, IV:9, and IV:10) and their mother (III:2). Paternal DNA (III:1)  
376 was not available.

377

378 *Cell culture*

379 HeLa cells (authenticated by ATCC through their human STR profiling cell authentication service), including  
380 Stx5ΔL cell lines, were maintained in high glucose DMEM with Glutamax (Gibco 31966021). Human primary  
381 dermal fibroblasts were obtained from patients or healthy donors and maintained in Medium 199 with EBSS  
382 and L-glutamine (Lonza BE12-119F). All media were supplemented with 10% fetal calf serum (FCS, Greiner Bio-

383 one, Kremsmünster, Austria) and antibiotic-antimycotic solution (Gibco 15240-062). All cells were regularly  
384 tested for mycoplasma contamination.

385

#### 386 *Plasmids and transfection*

387 Str-KDEL\_ManII-SBP-EGFP was a gift from Franck Perez (Addgene plasmid #65252;  
388 <http://n2t.net/addgene:65252>; RRID:Addgene\_65252). VAMP8-mCherry was constructed earlier<sup>36</sup> and  
389 previously deposited to Addgene (Addgene plasmid #92424). Str-KDEL\_Stx5L-SBP-mCitrine and Str-  
390 KDEL\_Stx5S-SBP-mCitrine were constructed by replacing the ManII-SBP-EGFP cassette in Str-KDEL\_ManII-SBP-  
391 EGFP using the *Ascl* and *XbaI* restriction sites. Stx5 coding sequences were codon-optimized for *Homo sapiens*  
392 using JCat and ordered from Genscript. Stx5LΔER coding sequence was generated with Q5-polymerase site-  
393 directed mutagenesis, using the Stx5L cDNA as a template with the following primer: 5'- CTTCG AATTC  
394 AATGA TTCCG GCCGC CGCCT ACGGC AGCAA GAACA CC. Sequences were verified with Sanger  
395 sequencing. HeLa cells were transfected with plasmid vectors using Fugene HD (Promega E2311), using the  
396 recommended protocol of the manufacturer. Only cells expressing low to moderate levels of the transfected  
397 plasmids, based on fluorescence intensity and manual localization scoring, were chosen for subsequent  
398 microscopic analyses.

399

#### 400 *CRISPR/Cas9*

401 Stable knock out of Stx5L in HeLa cells was obtained using the CRISPR-CAS9 method. For this, pairs of gRNA  
402 sequences were designed upstream of the STX5 initiation codon ([crispr.mit.edu](http://crispr.mit.edu), pair 1: ATAAC CTCGG ACTGT  
403 TGTGG AGG and ATGAT CCCGC GGAAA CGCTA CGG; pair 2: TAACC TCGGA CTGTT GTGGA GGG and TGATC  
404 CCGCG GAAAC GCTAC GGG). The gRNA sequences were cloned in pSpCas9n(BB)-2A-Puro (PX462) V2.0 (gift  
405 from Feng Zhang, Addgene no. 62987)<sup>76</sup> and transfected into HeLa cells by electroporation (Neon Transfection  
406 System, Thermofisher, MA). After initial selection with puromycin, the medium was changed for conditioned  
407 medium (collected from wildtype HeLa cells at 70% confluency) supplemented 1:1 with fresh medium. Single  
408 clones were obtained and screened for knockout of Stx5L by SDS-PAGE and Western blotting. Two clones  
409 (B1A7 and C1F4) were chosen for further experiments.

410

411 *Immunofluorescence*

412 Cells were plated on cleaned 12 mm glass coverslips (Electron Microscopy Services, 72230-01) and the  
413 following day fixed with 4% paraformaldehyde for 15 minutes at room temperature. Following quenching with  
414 50 mM NH<sub>4</sub>Cl in PBS, cells were permeabilized and blocked in 2% normal donkey serum (Rockland, 017-000-  
415 121) and 0.1% saponin (permeabilization buffer) for 30 mins at RT. Primary and secondary antibodies (list of  
416 antibodies and dilutions in Supplementary Table 5) were diluted in permeabilization buffer and incubated for 1  
417 hour at room temperature. Finally, cells were washed with 0.1% Triton X-100 in PBS to remove background  
418 staining and mounted with mounting medium containing 0.01% Trolox (6-hydroxy-2,5,7,8-  
419 tetramethylchroman-2-carboxylic acid) and 68% glycerol in 200 mM sodium phosphate buffer at pH 7.5 with  
420 0.1 µg/ml DAPI. Coverslips were sealed with nail polish. Cells were imaged on a Leica SP8 SMD confocal laser  
421 scanning microscope, equipped with an HC PL APO CS2 63x/1.20 WATER objective.

422

423 *Lectin stainings*

424 Cells were plated on cleaned 12 mm glass coverslips and after 72 hours culturing fixed with 4%  
425 paraformaldehyde. Cells were blocked with Carbo-Free Blocking solution (Vector Laboratories, SP-5040) and  
426 incubated with 4 µg/mL biotinylated SNA-I (Vector Laboratories, B-1305) or PNA (Vector Laboratories, B-1075)  
427 diluted in Carbo-Free Blocking solution. Cells were then incubated with Streptavidin-Alexa Fluor 647  
428 (ThermoScientific, S32357) before coverslips were mounted as described above. Cells were imaged on a Leica  
429 SP8 SMD confocal laser scanning microscope, equipped with an HC PL APO CS2 63x/1.20 WATER objective.

430

431 *Brefeldin A assay*

432 Fibroblasts were plated in black clear-bottom 96-wells plates (Greiner, 655090) and cultured until 80%  
433 confluent. Cells were either treated with 10 µg/mL Brefeldin A in DMSO (Cayman Chemicals, 11861) or DMSO  
434 alone for 15 minutes in a humidified incubator. After incubation, plates were transferred immediately to ice and  
435 cells were fixed with 4% paraformaldehyde, after which the above immunofluorescence protocol was  
436 performed. Microscopy images were acquired using a Leica high-content microscopy system based on a Leica  
437 DMI6000B (Leica Microsystems) and an HCX PL S-APO 40.0x0.75 DRY objective. HeLa cells were plated on 12  
438 mm coverslips and incubated in the same way with Brefeldin A, but fixed with 100% methanol at -20°C for 15  
439 mins. Imaging of these samples was performed using a Leica DMI6000B epifluorescence microscope equipped



440 with an HC PL APO 63x1.40 OIL objective. Cells were analyzed using Fiji (<http://fiji.sc/>) by first removing noise  
441 outliers (bright outliers, radius 2.0 pixels, threshold 50), then manually selecting cells and measuring the  
442 maximum fluorescence intensity in these ROIs. Data were normalized to the mean of the DMSO control of  
443 each group.

444

#### 445 *H-89 assay*

446 HeLa cells were plated on 12 mm coverslips and incubated the following day for 30 mins with 100  $\mu$ M H-89  
447 (Cayman Chemicals, 10010556) in DMSO or DMSO alone (vehicle) and H-89 was washed out with fresh  
448 medium for 5 mins. Cells were fixed with 4% paraformaldehyde for 15 mins at RT and permeabilized with  
449 100% methanol at -20°C for 15 mins prior to immunostaining with ERGIC53 mouse monoclonal antibody  
450 (G1/93 or OTI1A8) before epifluorescence imaging as described for the BFA assay. Cells were analyzed using  
451 Fiji and the number of ERGIC53-positive spots was quantified with the Spot Counter plugin. Data were  
452 normalized to the mean fluorescence of the DMSO control of each group. Data was analyzed with a Mann-  
453 Whitney U non-parametric test.

454

#### 455 *Transmission electron microscopy*

456 Fibroblasts were grown in 12-wells plates and fixed with 2% glutaraldehyde (Sigma-Aldrich, G5882) in PB (0.1  
457 M phosphate buffer, pH 7.4) for 60 mins at room temperature. Subsequently, cells were washed four times  
458 with PB and post-fixed with 1% osmium tetroxide and 1% potassium ferrocyanide in PB for 60 mins at room  
459 temperature. Then, cells were again washed four times with PB and dehydrated with graded steps of ethanol  
460 (30%, 50%, 70%, 96%, 100%) and embedded in Epon resin. 70 nm sections were cut with an ultramicrotome,  
461 then stained with 2% uranyl acetate solution and lead citrate solution. Stained sections were then examined  
462 using a JEOL JEM1400 transmission electron microscope.

463

#### 464 *Live-cell epifluorescence microscopy*

465 Cells were seeded in four-compartment dishes (Greiner 627870) and transfected as described above (3:1  
466 weight ratio reporter construct:Golgi label). Briefly before imaging, the culture medium was exchanged for  
467 Leibovitz's L-15 (Gibco 21083027). Samples were imaged using a DMI6000B (Leica Microsystems) with a  
468 heated stage (Pecon) and objective heater. All samples were imaged using an HC PL APO 63x/1.40–0.60 OIL

469 objective. VSVG-ts045-EGFP experiments were performed at 32°C after overnight incubation at 40°C, while all  
470 other epifluorescence experiments were performed at 37°C. For RUSH experiments, an equal amount of  
471 Leibovitz's L-15 supplemented with biotin was added to the well immediately before imaging, to reach a final  
472 concentration of 40 µM biotin. Live cell imaging was started immediately with 15 sec or 30 sec frame rates.  
473 Analysis was performed with Fiji, after registration of the image stacks, the increase in fluorescence was  
474 measured in the Golgi area by using the thresholded mScarlet-Giantin signal as an image mask.

475

#### 476 *FRET-FLIM*

477 All imaging took place in Leibovitz's L-15 supplemented with 10 µg/mL cycloheximide (Sigma-Aldrich, C4859)  
478 and cells were pulsed with biotin as described above. Imaging was performed on a Leica SP8 SMD system at  
479 37°C, equipped with an HC PL APO CS2 63x/1.20 WATER objective. Fluorophores were excited with a pulsed  
480 white light laser, operating at 80 MHz. mCitrine was excited at 514 nm, two separate HyD detectors were used  
481 to collect photons, set at 521-565 nm and 613-668 nm respectively. Photons were collected for one minute  
482 and lifetime histograms of the donor fluorophore were fitted with monoexponential decay functions  
483 convoluted with the microscope instrument response function in Leica LAS X.

#### 484 *Immunoprecipitation*

485 HeLa cells were lysed 48 hours post-transfection with IP lysis buffer (20 mM Tris-HCl pH 7.6, 137 mM NaCl, 1%  
486 IGEPAL, 2 mM EDTA and complete protease inhibitors (Roche 5892791001)). Protein levels were equilibrated  
487 and lysates were immunoprecipitated with 1 µg anti-GFP-antibody (Rockland 600-401-215) and protein A  
488 beads (ThermoFisher, 20333) for 1 hour at 4°C with constant agitation. After three washes with IP lysis buffer,  
489 samples were boiled in 5x SDS sample buffer with β-mercaptoethanol and resolved with SDS-PAGE and  
490 subsequent immunoblotting.

491

#### 492 *SDS-PAGE and immunoblotting*

493 Cells were plated in 12-wells plates in culture medium and lysed the following day with SDS lysis buffer (1%  
494 SDS, 10 mM Tris-HCl pH 6.8). Lysates were diluted to equal protein content (30 µg per lane) with SDS lysis  
495 buffer, separated with SDS-PAGE on 4–20% Mini-PROTEAN TGX Precast Protein Gels (Biorad, 4561094) and  
496 subsequently transferred onto 0.45 µm PVDF membranes. Small molecular weight proteins (Bet1 and Bet1L)  
497 were separated on 16% Schaeffer gels<sup>77</sup>.

498

499 *Quantification and statistical analysis*

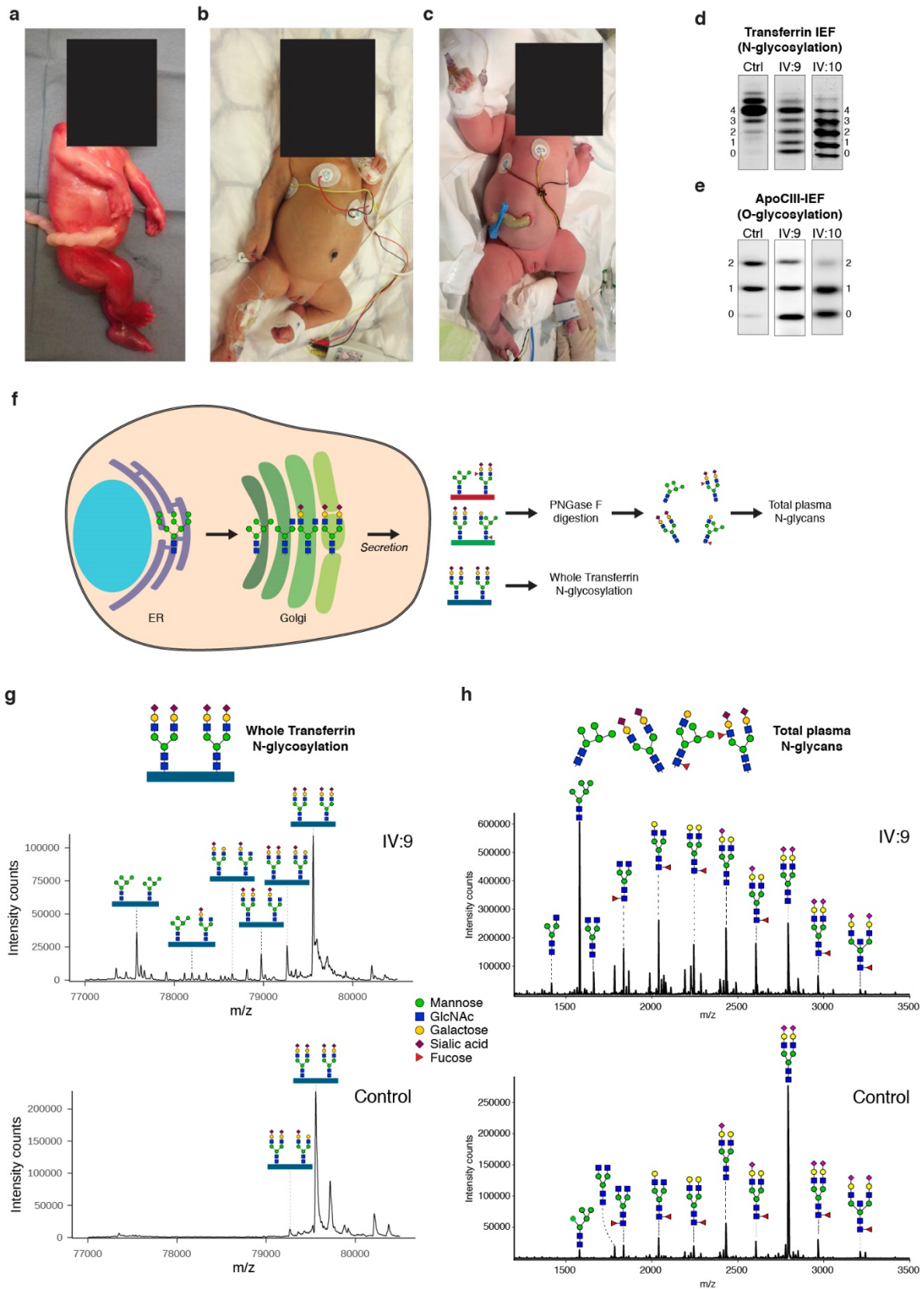
500 All mean values represent the average of all cells analyzed. All comparisons between two groups were first  
501 checked for similar mean and median values and acceptable (< 3x) difference in variance, before statistical  
502 analysis with an unpaired two-sided Student's t-test. Relative intensity data was first transformed using the  
503 binary logarithm before analysis with an unpaired two-sided Student's t-test. H-89 data was analyzed with a  
504 Mann-Whitney U non-parametric test. Stx5 kinetics data were analyzed with a one-way ANOVA, followed by a  
505 posthoc Tukey's honestly significant difference test. Stx5 FLIM data were analyzed with a two-way ANOVA,  
506 with the isoform and timepoint as independent variables, followed by a posthoc Tukey's honestly significant  
507 difference test.  $p < 0.05$  was considered significant. \* $p < 0.05$ , \*\* $p < 0.01$ , \*\*\* $p < 0.001$ , \*\*\*\* $p \leq 0.0001$ . All  
508 statistical analyses were performed using R statistical software. All numerical data were visualized using R  
509 package *ggplot2*<sup>78</sup>, with violins representing the overall distribution of the data and means  $\pm$  95% CI overlaid.

510

511 *Data and code availability*

512 Microarray data, exome sequencing data and ImageJ macros for quantification of the RUSH experiments are  
513 available upon request.

514 Figures



515 **Figure 1. A novel, lethal, genetic variant suggests a defect in protein glycosylation related to Golgi**  
516 **trafficking.**

517 (a-c) Clinical images of Stx5M55V patients IV:8 (a), IV:9 (b), IV:10 (c).

518 (d) Glycosylation screening by isoelectric focusing (IEF) of serum transferrin. The accompanying numbers  
519 represent the total number of sialic acids in the different proteoforms. Both patients show a reduction in the  
520 number of sialic acids.

521 (e) Glycosylation screening by IEF of serum Apolipoprotein C3 (ApoCIII). ApoCIII has one mucin-type O-linked  
522 glycan with one or two sialic acids in controls. Both patients show a reduction in the number of sialic acids.

523 (f) Schematic overview of N-glycosylation intermediates in the Golgi. For mass spectrometry analysis of glycan  
524 structures, glycosylated transferrin is enriched from all secreted glycoproteins in human serum and subjected  
525 to intact protein mass spectrometry. In parallel, a different serum sample is treated with PNGase F to cleave  
526 and analyze N-glycans from all plasma proteins.

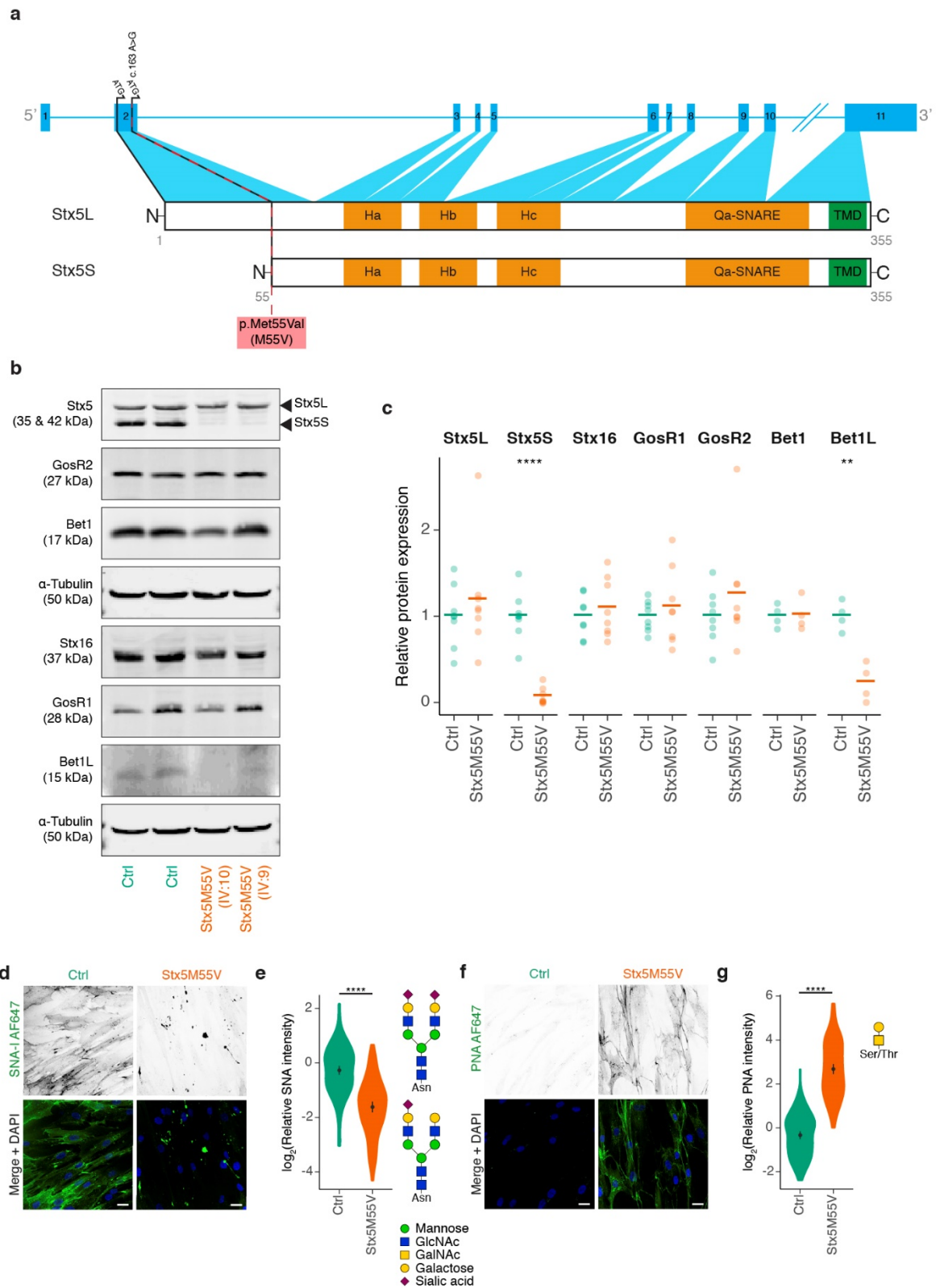
527 (g) Nanochip-C8 QTOF mass spectra of enriched intact serum Transferrin of Stx5M55V patient IV:9 (top  
528 spectrum) and healthy control (lower spectrum) are shown. Key transferrin glycoforms are shown, indicating a  
529 strong increase of high-mannose glycans and glycans lacking sialic acid and galactose. Annotation of all peaks  
530 of patients IV:9 and IV:10 is shown in [Supplementary Table 2](#).

531 (h) MALDI-TOF mass spectra of total plasma N-glycans of Stx5M55V patient IV:9 (top spectrum) and healthy  
532 control (lower spectrum) are shown. Structural analysis shows a strong increase of high-mannose glycans and  
533 glycans lacking sialic acid and galactose. Annotation of all peaks of patients IV:9 and IV:10 is shown in

534 [Supplementary Table 3](#).

535

536



537

538 **Figure 2. Primary dermal fibroblasts are an accurate model of the glycosylation defect observed in**  
539 **Stx5M55V patients.**

540 (a) Schematic representation of the intron-exon structure of *STX5* and the encoded proteoforms resulting from  
541 the two starting codons in exon 2. The Stx5M55V genetic variant is indicated by a dashed red line. Orange  
542 regions have a secondary helical structure. TMD, transmembrane domain. Ha, Hb, Hc: regulatory Habc-domain

543 (b) Representative immunoblot for SNARE proteins of cell lysates of primary human dermal fibroblasts of  
544 healthy donors (green, Ctrl) or Stx5M55V patients (orange, Stx5M55V).  $\alpha$ -Tubulin, loading control.

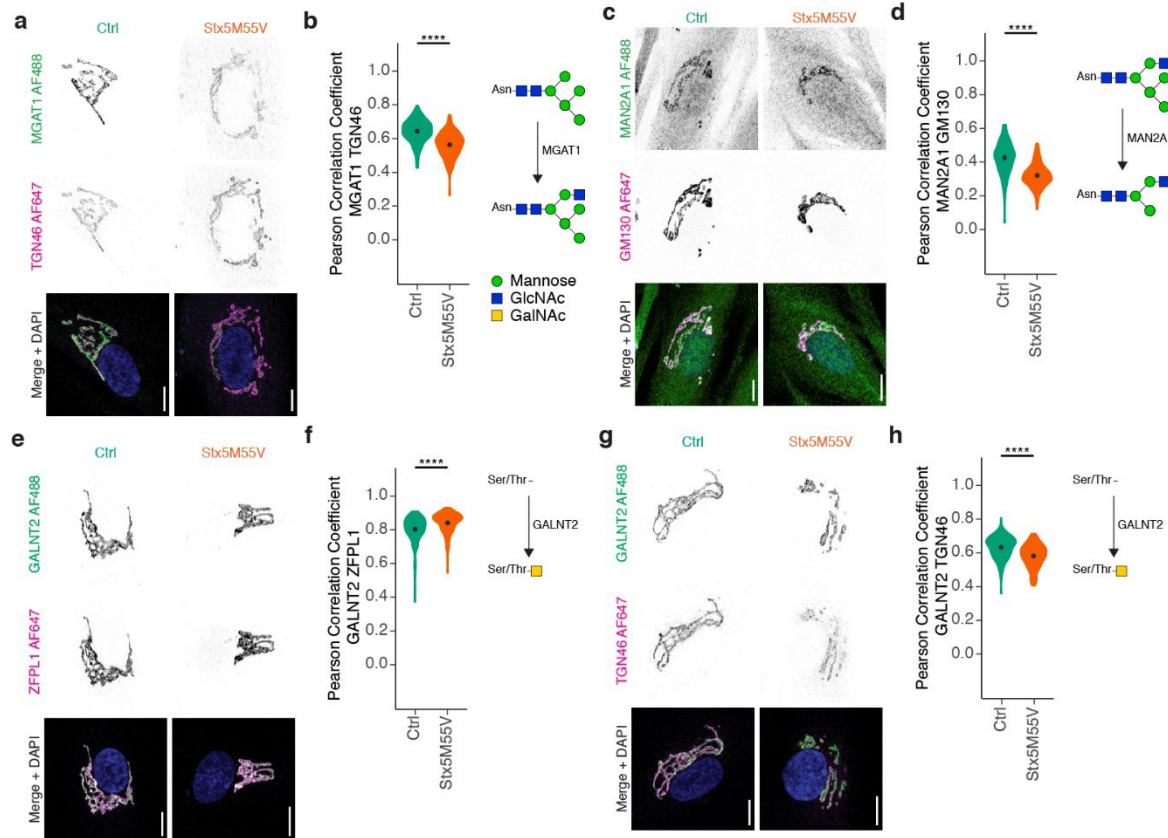
545 (c) Quantification of (b). Protein levels were first normalized to the loading control, then to the average  
546 expression of both control lines. Each point represents one cell line from 2 independent experiments.

547 (d) Fibroblasts of healthy donors (green, Ctrl) or Stx5M55V patients (orange, Stx5M55V) were probed with  
548 SNA-I lectin (green in merge). Representative confocal micrographs. Scalebars, 25  $\mu$ m. DAPI in blue.

549 (e) Quantification of (d). All data were normalized to the healthy donor and then  $\log_2$ -transformed. N = 124  
550 (Ctrl) and 111 (Stx5M55V) cells from 2 independent experiments.

551 (f-g) Same as panels (d-e), but now for PNA lectin. N = 117 (Ctrl) and 122 (Stx5M55V) cells from 2 independent  
552 experiments.

553



554

555 **Figure 3. Glycosylation enzymes mislocalize in Stx5M55V patient fibroblasts.**

556 (a) Immunofluorescence microscopy of MGAT1 (green in merge) and TGN46 (magenta) in primary dermal  
 557 fibroblasts of healthy donors (green, Ctrl) or Stx5M55V patients (orange, Stx5M55V). Representative confocal  
 558 micrographs. Scalebars, 10  $\mu$ m. DAPI in blue.

559 (b) Pearson's correlations coefficients between MGAT1 and TGN46 of panel (a). N = 157 (Ctrl) and 162  
 560 (Stx5M55V) cells from 2 independent experiments.

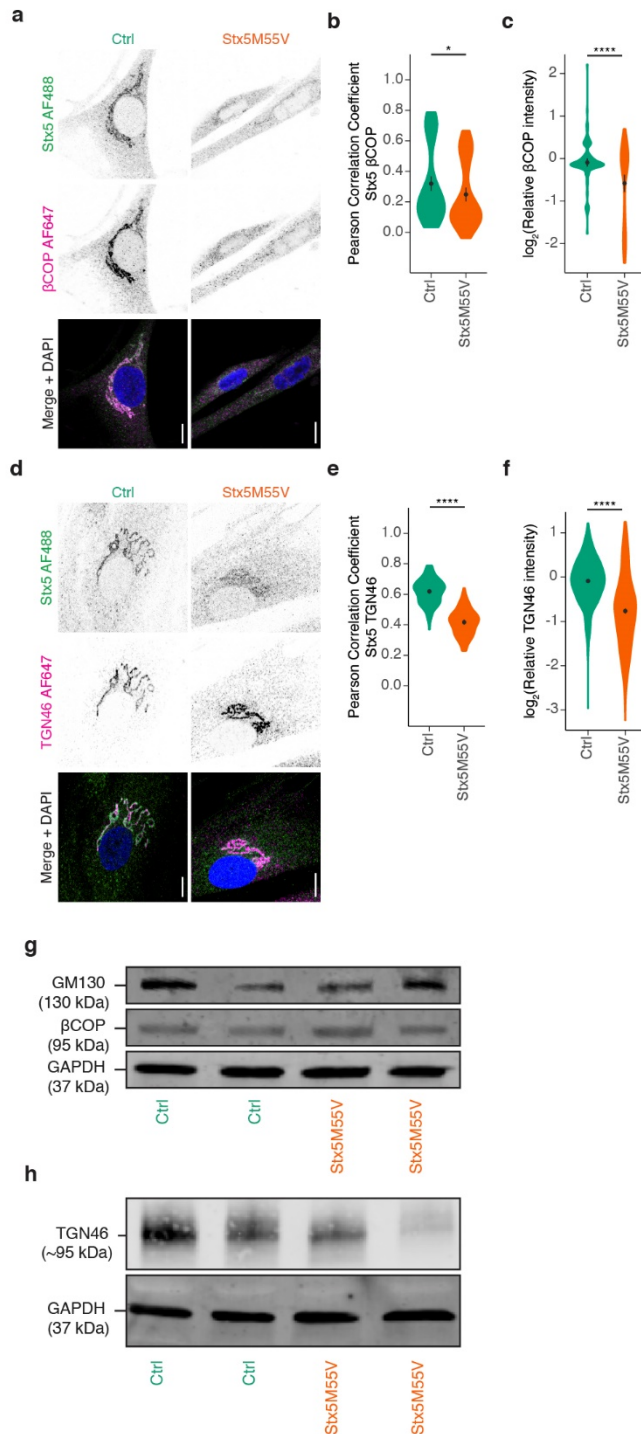
561 (c-d) Same as panels (a-b), but now for MAN2A1 (green) and GM130 (magenta). N = 127 (Ctrl) and 143  
 562 (Stx5M55V) cells from 2 independent experiments.

563 (e-f) Same as panels (a-b), but now for GALNT2 (green) and ZFPL1 (magenta). N = 240 (Ctrl) and 146  
 564 (Stx5M55V) cells from 2 independent experiments.

565 (g-h) Same as panels (a-b), but now for GALNT2 (green) and TGN46 (magenta). N = 172 (Ctrl) and 152  
 566 (Stx5M55V) cells from 2 independent experiments.

567

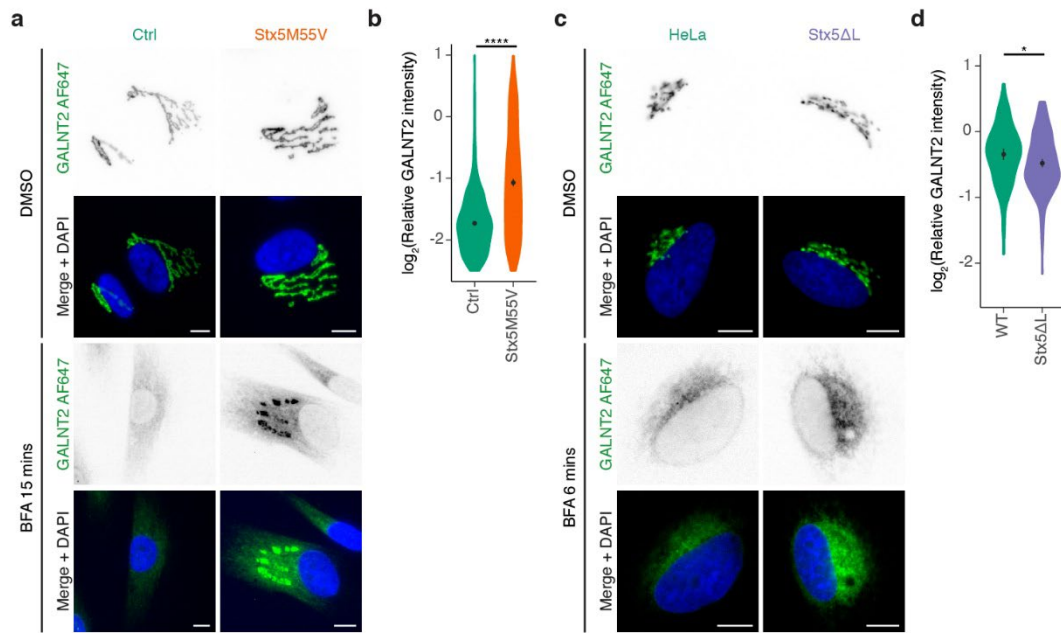




568 **Figure 4. Reduced localization of Stx5 to trans-Golgi network in Stx5M55V patients.**

569 (a) Immunofluorescence microscopy of Stx5 (green in merge) and  $\beta$ COP (magenta) in primary dermal  
 570 fibroblasts of healthy donors (green, Ctrl) or Stx5M55V patients (orange, Stx5M55V). Representative confocal  
 571 micrographs. Scalebars, 10  $\mu$ m. DAPI in blue.

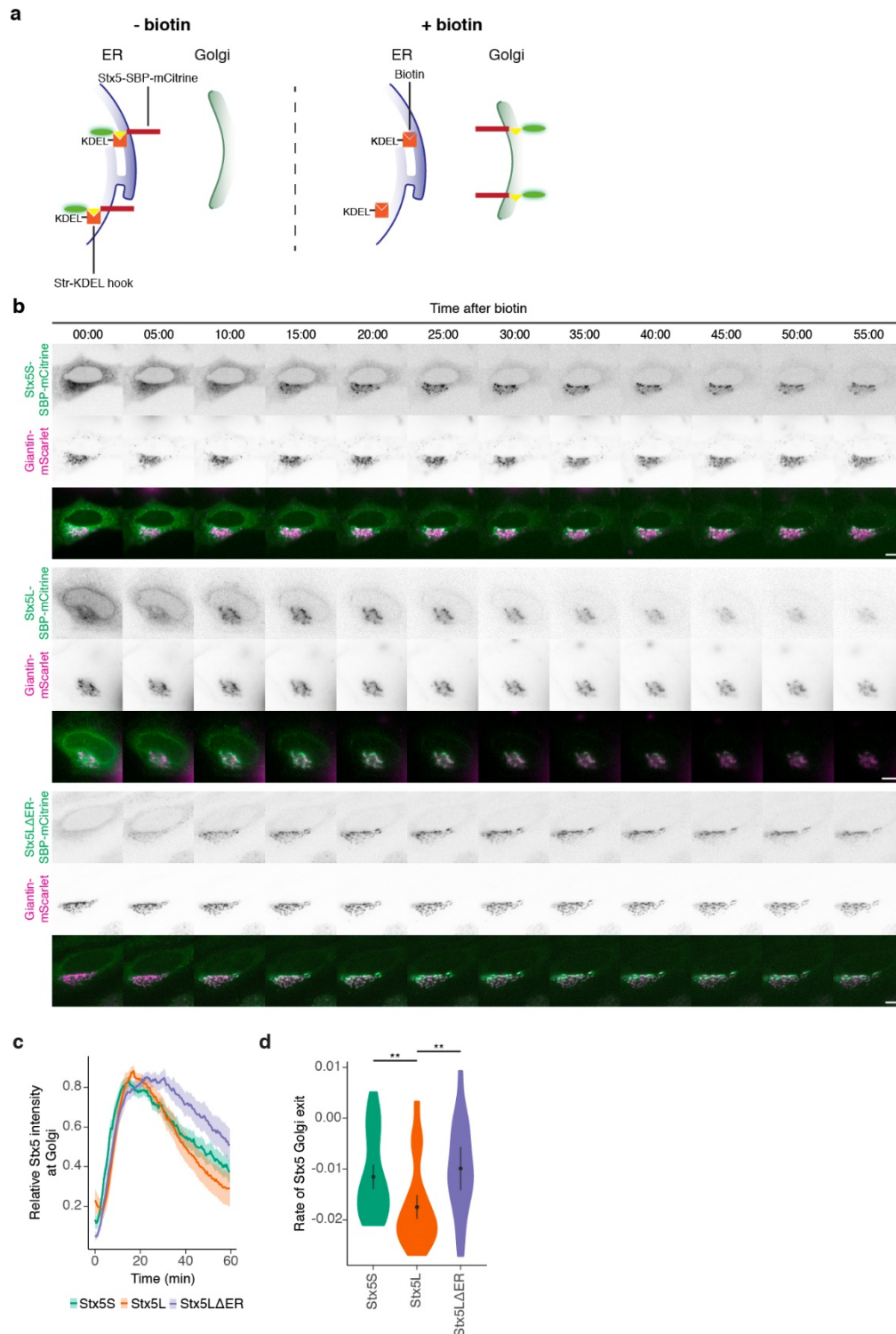
- 572 (b) Pearson's correlations coefficients between Stx5 and  $\beta$ COP of panel (a). N = 109 (Ctrl) and 87 (Stx5M55V)  
573 cells from 2 independent experiments.
- 574 (c) Fluorescence intensities of  $\beta$ COP from panel (a) relative to the healthy control. N = 109 (Ctrl) and 87  
575 (Stx5M55V) cells from 2 independent experiments.
- 576 (d-f) Same as panels (a-c), but now for Stx5 (green) and TGN46 (magenta). N = 128 (Ctrl) and 114 (Stx5M55V)  
577 cells from 2 independent experiments for colocalization, N = 822 (Ctrl) and 783 (Stx5M55V) cells from 6  
578 independent experiments for intensity.
- 579 (g) Representative immunoblot for GM130 and  $\beta$ COP of the cells from panel A. GAPDH, loading control.
- 580 (h) Same as panel (g), but now for TGN46.
- 581



582 **Figure 5. Loss of Stx5S inhibits ER-Golgi trafficking, while the loss of Stx5L accelerates ER-Golgi trafficking.**

583 (a) Immunofluorescence microscopy of GALNT2 (green in merge) in primary human dermal fibroblasts of  
584 healthy donors (green, Ctrl) or Stx5M55V patients (orange, Stx5M55V) in the absence or presence of Brefeldin  
585 A (BFA) for 15 min. Representative epifluorescence micrographs are shown. Scalebars, 10  $\mu$ m. DAPI in blue.  
586 (b) Relative maximum fluorescence intensities of GALNT2 from panel (A). All data were normalized to the  
587 DMSO condition (vehicle). N = 979 (Ctrl) and 943 (Stx5M55V) cells from 2 independent experiments.  
588 (c-d) Same as panels (a-b) B, but now in parental HeLa and Stx5ΔL lines with only 6 min BFA treatment. N = 103  
589 (WT) and 212 (Stx5ΔL) cells from 2 independent experiments.

590



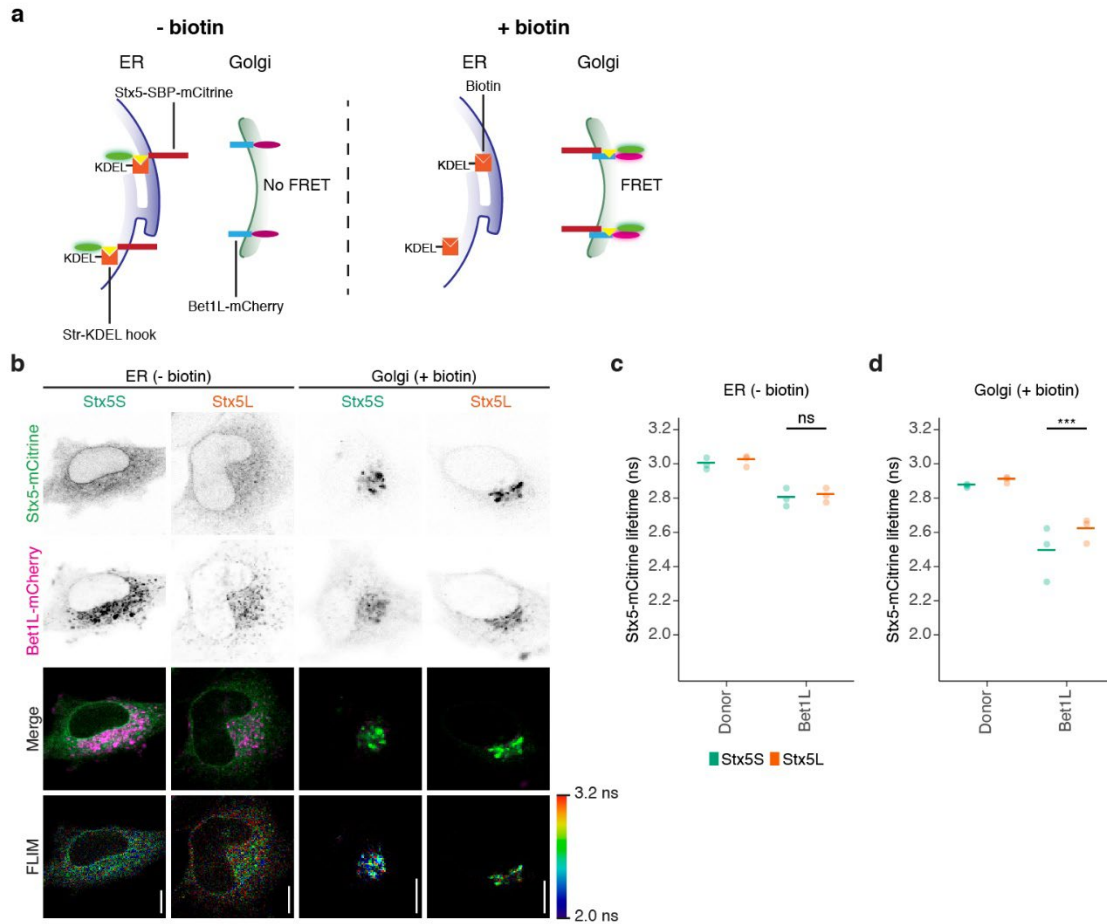
591 **Figure 6. Faster Golgi transit of Stx5L than Stx5S**

592 (a) Schematic overview of the design of Stx5 trafficking experiment, based on the RUSH system. In absence of  
593 biotin (left panel), the reporter cargo (Stx5-SBP-mCitrine) is trapped at the ER by the luminal Str-KDEL hook.

594 When biotin is added (right panel), biotin outcompetes the interaction with streptavidin, allowing Stx5-SBP-  
595 mCitrine to traffic freely to its destination compartment. SBP, streptavidin binding protein; Str, streptavidin.  
596 (b) Snapshots of live-cell imaging of Stx5-SBP-mCitrine (green in merge). Magenta: Golgi marker Giantin-  
597 mScarlet. Scale bars, 10  $\mu$ m. See also supplementary movies 5 – 7.

598 (c) Quantification of mCitrine fluorescence at the Golgi of Stx5S-SBP-mCitrine (green), Stx5L-SBP-mCitrine  
599 (orange) and Stx5 $\Delta$ ER-SBP-mCitrine (blue) over time from panel (b). N = 44 (Stx5S), 47 (Stx5L) and 19  
600 (Stx5 $\Delta$ ER) cells from 4 independent experiments.

601 (d) Quantification of the slopes from panel (c) of the post-Golgi section (~20 mins onwards).  
602



603

604 **Figure 7. Stx5S is the dominant Qa-SNARE for intra-Golgi trafficking**

605 (a) Schematic overview of experimental design for complex formation of Stx5 isoforms with Bet1L, based on  
 606 the RUSH system and SNARE complex measurement by FRET-FLIM. In absence of biotin (left panel), the  
 607 reporter cargo (Stx5-SBP-mCitrine) is trapped at the ER by the luminal Str-KDEL hook, and no FRET with Golgi-  
 608 localized Bet1L-mCherry can occur. When biotin is added (right panel), biotin outcompetes the interaction  
 609 with streptavidin, allowing Stx5-SBP-mCitrine to traffic freely to its destination compartment, and SNARE  
 610 complex formation with Golgi-localized Bet1L-mCherry can occur resulting in FRET. SBP, streptavidin binding  
 611 protein; Str, streptavidin; FRET, Förster resonant energy transfer. FLIM, fluorescence lifetime imaging  
 612 microscopy.

613 (b) Representative confocal micrographs of HeLa cells co-expressing Stx5-mCitrine (green in merge) and Bet1L-  
 614 mCherry (magenta) without (ER) or with (Golgi) biotin. Scalebars, 10 μm.

615 (c-d) Average fluorescence lifetimes at the ER (c) and Golgi (d) from panel (b). N = 52 (Stx5S Donor ER), 74

616 (Stx5L Donor ER), 47 (Stx5S Bet1L ER), 51 (Stx5L Bet1L ER), 50 (Stx5S Donor Golgi), 71 (Stx5L Donor Golgi), 58

617 (Stx5S Bet1L Golgi) and 58 (Stx5L Bet1L Golgi) cells from 3 independent experiments. Each point represents  
618 one independent experiment.

619 **References**

- 620 1. Bentley, M. *et al.* SNARE status regulates tether recruitment and function in homotypic COPII vesicle  
621 fusion. *The Journal of biological chemistry* **281**, 38825–33 (2006).
- 622 2. Dascher, C., Matteson, J. & Balch, W. E. Syntaxin 5 regulates endoplasmic reticulum to Golgi transport.  
623 *The Journal of biological chemistry* **269**, 29363–6 (1994).
- 624 3. Rowe, T., Dascher, C., Bannykh, S., Plutner, H. & Balch, W. E. Role of vesicle-associated syntaxin 5 in the  
625 assembly of pre-Golgi intermediates. *Science (New York, N.Y.)* **279**, 696–700 (1998).
- 626 4. Xu, D., Joglekar, A. P., Williams, A. L. & Hay, J. C. Subunit structure of a mammalian ER/Golgi SNARE  
627 complex. *The Journal of biological chemistry* **275**, 39631–9 (2000).
- 628 5. Hay, J. C. *et al.* Localization, Dynamics, and Protein Interactions Reveal Distinct Roles for ER and Golgi  
629 SNAREs. *The Journal of Cell Biology* **141**, 1489–1502 (1998).
- 630 6. Paek, I. *et al.* ERS-24, a Mammalian v-SNARE Implicated in Vesicle Traffic between the ER and the Golgi.  
631 *The Journal of Cell Biology* **137**, 1017–1028 (1997).
- 632 7. Zhang, T. *et al.* Ykt6 forms a SNARE complex with syntaxin 5, GS28, and Bet1 and participates in a late  
633 stage in endoplasmic reticulum-Golgi transport. *The Journal of biological chemistry* **276**, 27480–7 (2001).
- 634 8. Jahn, R. & Scheller, R. H. SNAREs — engines for membrane fusion. *Nature Reviews Molecular Cell Biology*  
635 **7**, 631–631 (2006).
- 636 9. Banfield, D. K., Lewis, M. J. & Pelham, H. R. B. A SNARE-like protein required for traffic through the Golgi  
637 complex. *Nature* **375**, 806–809 (1995).
- 638 10. Parlati, F. *et al.* Topological restriction of SNARE-dependent membrane fusion. *Nature* **407**, 194–198  
639 (2000).
- 640 11. Parlati, F. *et al.* Distinct SNARE complexes mediating membrane fusion in Golgi transport based on  
641 combinatorial specificity. *Proceedings of the National Academy of Sciences of the United States of America*  
642 **99**, 5424–9 (2002).
- 643 12. Xu, Y., Martin, S., James, D. E. & Hong, W. GS15 Forms a SNARE Complex with Syntaxin 5, GS28, and Ykt6  
644 and Is Implicated in Traffic in the Early Cisternae of the Golgi Apparatus. *MBoC* **13**, 3493–3507 (2002).
- 645 13. Linders, P. T., van der Horst, C., ter Beest, M. & van den Bogaart, G. Stx5-Mediated ER-Golgi Transport in  
646 Mammals and Yeast. *Cells* **8**, 780 (2019).



- 647 14. Malsam, J. & Söllner, T. H. Organization of SNAREs within the Golgi stack. *Cold Spring Harbor perspectives*  
648 *in biology* **3**, a005249–a005249 (2011).
- 649 15. Tai, G. *et al.* Participation of the Syntaxin 5/Ykt6/GS28/GS15 SNARE Complex in Transport from the  
650 Early/Recycling Endosome to the Trans-Golgi Network. *MBoC* **15**, 4011–4022 (2004).
- 651 16. Dickinson, M. E. *et al.* High-throughput discovery of novel developmental phenotypes. *Nature* **537**, 508–  
652 514 (2016).
- 653 17. Koscielny, G. *et al.* The International Mouse Phenotyping Consortium Web Portal, a unified point of access  
654 for knockout mice and related phenotyping data. *Nucleic Acids Res* **42**, D802–D809 (2014).
- 655 18. Hui, N. *et al.* An isoform of the Golgi t-SNARE, syntaxin 5, with an endoplasmic reticulum retrieval signal.  
656 *Molecular biology of the cell* **8**, 1777–87 (1997).
- 657 19. Gao, G. & Banfield, D. K. Multiple features within the syntaxin Sed5p mediate its Golgi localization. *Traffic*  
658 **21**, 274–296 (2020).
- 659 20. Dominguez, M. *et al.* gp25L/emp24/p24 protein family members of the cis-Golgi network bind both COP I  
660 and II coatomer. *The Journal of cell biology* **140**, 751–65 (1998).
- 661 21. Miyazaki, K. *et al.* Contribution of the long form of syntaxin 5 to the organization of the endoplasmic  
662 reticulum. *Journal of Cell Science* **125**, 5658 LP – 5666 (2012).
- 663 22. Suga, K., Saito, A., Tomiyama, T., Mori, H. & Akagawa, K. The Syntaxin 5 Isoforms Syx5 and Syx5L have  
664 Distinct Effects on the Processing of  $\beta$ -amyloid Precursor Protein. *The Journal of Biochemistry* **146**, 905–  
665 915 (2009).
- 666 23. Avci, D. *et al.* The intramembrane protease SPP impacts morphology of the endoplasmic reticulum by  
667 triggering degradation of morphogenic proteins. *J. Biol. Chem.* **294**, 2786–2800 (2019).
- 668 24. Hay, J. C., Hirling, H. & Scheller, R. H. Mammalian vesicle trafficking proteins of the endoplasmic reticulum  
669 and Golgi apparatus. *J. Biol. Chem.* **271**, 5671–5679 (1996).
- 670 25. Shestakova, A., Suvorova, E., Pavliv, O., Khaidakova, G. & Lupashin, V. Interaction of the conserved  
671 oligomeric Golgi complex with t-SNARE Syntaxin5a/Sed5 enhances intra-Golgi SNARE complex stability.  
672 *The Journal of Cell Biology* **179**, 1179–1192 (2007).
- 673 26. Zhang, T. *et al.* The Mammalian Protein (rbet1) Homologous to Yeast Bet1p Is Primarily Associated with  
674 the Pre-Golgi Intermediate Compartment and Is Involved in Vesicular Transport from the Endoplasmic  
675 Reticulum to the Golgi Apparatus. *The Journal of Cell Biology* **139**, 1157–1168 (1997).

- 676 27. Mallard, F. *et al.* Early/recycling endosomes-to-TGN transport involves two SNARE complexes and a Rab6  
677 isoform. *The Journal of Cell Biology* **156**, 653–664 (2002).
- 678 28. Dingjan, I. *et al.* Endosomal and Phagosomal SNAREs. *Physiological Reviews* **98**, 1465–1492 (2018).
- 679 29. Chiu, C.-F. *et al.* ZFPL1, a novel ring finger protein required for cis-Golgi integrity and efficient ER-to-Golgi  
680 transport. *The EMBO journal* **27**, 934–47 (2008).
- 681 30. Jaiman, A. & Thattai, M. Algorithmic biosynthesis of eukaryotic glycans. *bioRxiv* 440792 (2018)  
682 doi:10.1101/440792.
- 683 31. Glick, B. S. & Nakano, A. Membrane Traffic Within the Golgi Apparatus. *Annual Review of Cell and*  
684 *Developmental Biology* **25**, 113–132 (2009).
- 685 32. Galea, G., Bexiga, M. G., Panarella, A., O’Neill, E. D. & Simpson, J. C. A high-content screening microscopy  
686 approach to dissect the role of Rab proteins in Golgi-to-ER retrograde trafficking. *J Cell Sci* **128**, 2339–2349  
687 (2015).
- 688 33. Boncompain, G. *et al.* Synchronization of secretory protein traffic in populations of cells. *Nature Methods*  
689 **9**, 493–493 (2012).
- 690 34. Lippincott-Schwartz, J., Roberts, T. H. & Hirschberg, K. Secretory Protein Trafficking and Organelle  
691 Dynamics in Living Cells. *Annual Review of Cell and Developmental Biology* **16**, 557–589 (2000).
- 692 35. Bindels, D. S. *et al.* mScarlet: a bright monomeric red fluorescent protein for cellular imaging. *Nature*  
693 *Methods* **14**, 53–56 (2017).
- 694 36. Verboogen, D. R. J., González Mancha, N., ter Beest, M. & van den Bogaart, G. Fluorescence Lifetime  
695 Imaging Microscopy reveals rerouting of SNARE trafficking driving dendritic cell activation. *eLife* **6**, (2017).
- 696 37. Griesbeck, O., Baird, G. S., Campbell, R. E., Zacharias, D. A. & Tsien, R. Y. Reducing the Environmental  
697 Sensitivity of Yellow Fluorescent Protein MECHANISM AND APPLICATIONS. *J. Biol. Chem.* **276**, 29188–  
698 29194 (2001).
- 699 38. Casey, J. R., Grinstein, S. & Orlowski, J. Sensors and regulators of intracellular pH. *Nature reviews.*  
700 *Molecular cell biology* **11**, 50–61 (2010).
- 701 39. Antonin, W., Holroyd, C., Tikkanen, R., Höning, S. & Jahn, R. The R-SNARE Endobrevin/VAMP-8 Mediates  
702 Homotypic Fusion of Early Endosomes and Late Endosomes. *MBoC* **11**, 3289–3298 (2000).
- 703 40. Bajno, L. *et al.* Focal Exocytosis of Vamp3-Containing Vesicles at Sites of Phagosome Formation. *J Cell Biol*  
704 **149**, 697–706 (2000).

- 705 41. Hong, W. SNAREs and traffic. *Biochimica et Biophysica Acta (BBA) - Molecular Cell Research* **1744**, 120–  
706 144 (2005).
- 707 42. Manderson, A. P., Kay, J. G., Hammond, L. A., Brown, D. L. & Stow, J. L. Subcompartments of the  
708 macrophage recycling endosome direct the differential secretion of IL-6 and TNF $\alpha$ . *J Cell Biol* **178**, 57–69  
709 (2007).
- 710 43. Murray, R. Z. A Role for the Phagosome in Cytokine Secretion. *Science* **310**, 1492–1495 (2005).
- 711 44. Amberger, J. S., Bocchini, C. A., Schiettecatte, F., Scott, A. F. & Hamosh, A. OMIM.org: Online Mendelian  
712 Inheritance in Man (OMIM<sup>®</sup>), an online catalog of human genes and genetic disorders. *Nucleic Acids Res*  
713 **43**, D789–D798 (2015).
- 714 45. Pedersen, A. G. & Nielsen, H. Neural network prediction of translation initiation sites in eukaryotes:  
715 perspectives for EST and genome analysis. *Proc Int Conf Intell Syst Mol Biol* **5**, 226–233 (1997).
- 716 46. Kochetov, A. V. Alternative translation start sites and hidden coding potential of eukaryotic mRNAs.  
717 *BioEssays* **30**, 683–691 (2008).
- 718 47. Kozak, M. Regulation of translation via mRNA structure in prokaryotes and eukaryotes. *Gene* **361**, 13–37  
719 (2005).
- 720 48. Oka, T., Ungar, D., Hughson, F. M. & Krieger, M. The COG and COPI Complexes Interact to Control the  
721 Abundance of GEARs, a Subset of Golgi Integral Membrane Proteins. *MBoC* **15**, 2423–2435 (2004).
- 722 49. Ohtsubo, K. & Marth, J. D. Glycosylation in Cellular Mechanisms of Health and Disease. *Cell* **126**, 855–867  
723 (2006).
- 724 50. Freeze, H. H., Chong, J. X., Bamshad, M. J. & Ng, B. G. Solving Glycosylation Disorders: Fundamental  
725 Approaches Reveal Complicated Pathways. *The American Journal of Human Genetics* **94**, 161–175 (2014).
- 726 51. Fisher, P. & Ungar, D. Bridging the Gap between Glycosylation and Vesicle Traffic. *Front. Cell Dev. Biol.* **4**,  
727 (2016).
- 728 52. Blackburn, J. B., Kudlyk, T., Pokrovskaya, I. & Lupashin, V. V. More than just sugars: Conserved oligomeric  
729 Golgi complex deficiency causes glycosylation-independent cellular defects. *Traffic* **19**, 463–480 (2018).
- 730 53. Foulquier, F. *et al.* Conserved oligomeric Golgi complex subunit 1 deficiency reveals a previously  
731 uncharacterized congenital disorder of glycosylation type II. *PNAS* **103**, 3764–3769 (2006).
- 732 54. Foulquier, F. *et al.* A new inborn error of glycosylation due to a Cog8 deficiency reveals a critical role for  
733 the Cog1–Cog8 interaction in COG complex formation. *Hum Mol Genet* **16**, 717–730 (2007).

- 734 55. Kranz, C. *et al.* COG8 deficiency causes new congenital disorder of glycosylation type IIh. *Hum Mol Genet*  
735 **16**, 731–741 (2007).
- 736 56. Miller, V. J. & Ungar, D. Re‘COG’niton at the Golgi. *Traffic* **13**, 891–897 (2012).
- 737 57. Morava, E. *et al.* A common mutation in the COG7 gene with a consistent phenotype including  
738 microcephaly, adducted thumbs, growth retardation, VSD and episodes of hyperthermia. *Eur J Hum Genet*  
739 **15**, 638–645 (2007).
- 740 58. Ng, B. G. *et al.* Molecular and clinical characterization of a Moroccan Cog7 deficient patient. *Molecular*  
741 *Genetics and Metabolism* **91**, 201–204 (2007).
- 742 59. Reynders, E. *et al.* Golgi function and dysfunction in the first COG4-deficient CDG type II patient. *Hum Mol*  
743 *Genet* **18**, 3244–3256 (2009).
- 744 60. Wu, X. *et al.* Mutation of the COG complex subunit gene COG7 causes a lethal congenital disorder. *Nat*  
745 *Med* **10**, 518–523 (2004).
- 746 61. Huchtagowder, V. *et al.* Loss-of-function mutations in ATP6V0A2 impair vesicular trafficking, tropoelastin  
747 secretion and cell survival. *Hum Mol Genet* **18**, 2149–2165 (2009).
- 748 62. Jansen, J. C. *et al.* CCDC115 Deficiency Causes a Disorder of Golgi Homeostasis with Abnormal Protein  
749 Glycosylation. *The American Journal of Human Genetics* **98**, 310–321 (2016).
- 750 63. Jansen, J. C. *et al.* TMEM199 Deficiency Is a Disorder of Golgi Homeostasis Characterized by Elevated  
751 Aminotransferases, Alkaline Phosphatase, and Cholesterol and Abnormal Glycosylation. *The American*  
752 *Journal of Human Genetics* **98**, 322–330 (2016).
- 753 64. Jansen, E. J. R. *et al.* ATP6AP1 deficiency causes an immunodeficiency with hepatopathy, cognitive  
754 impairment and abnormal protein glycosylation. *Nature Communications* **7**, 11600–11600 (2016).
- 755 65. Foulquier, F. *et al.* TMEM165 Deficiency Causes a Congenital Disorder of Glycosylation. *The American*  
756 *Journal of Human Genetics* **91**, 15–26 (2012).
- 757 66. Ashikov, A. *et al.* Integrating glycomics and genomics uncovers SLC10A7 as essential factor for bone  
758 mineralization by regulating post-Golgi protein transport and glycosylation. *Hum Mol Genet* **27**, 3029–  
759 3045 (2018).
- 760 67. Park, J. H. *et al.* SLC39A8 Deficiency: A Disorder of Manganese Transport and Glycosylation. *The American*  
761 *Journal of Human Genetics* **97**, 894–903 (2015).

- 762 68. Witkos, T. M. *et al.* GORAB scaffolds COPI at the trans -Golgi for efficient enzyme recycling and correct  
763 protein glycosylation. *Nat Commun* **10**, 1–18 (2019).
- 764 69. Zhong, W. Golgi during Development. *Cold Spring Harb Perspect Biol* **3**, (2011).
- 765 70. Zhao, H. Membrane Trafficking in Osteoblasts and Osteoclasts: New Avenues for Understanding and  
766 Treating Skeletal Diseases. *Traffic* **13**, 1307–1314 (2012).
- 767 71. Wagner, T., Dieckmann, M., Jaeger, S., Weggen, S. & Pietrzik, C. U. Stx5 is a novel interactor of VLDL-R to  
768 affect its intracellular trafficking and processing. *Experimental Cell Research* **319**, 1956–1972 (2013).
- 769 72. Morelle, W. & Michalski, J.-C. Analysis of protein glycosylation by mass spectrometry. *Nature Protocols* **2**,  
770 1585–1602 (2007).
- 771 73. Scherpenzeel, M. van, Steenbergen, G., Morava, E., Wevers, R. A. & Lefeber, D. J. High-resolution mass  
772 spectrometry glycoprofiling of intact transferrin for diagnosis and subtype identification in the congenital  
773 disorders of glycosylation. *Translational Research* **166**, 639-649.e1 (2015).
- 774 74. Vissers, L. E. L. M. *et al.* A de novo paradigm for mental retardation. *Nature Genetics* **42**, 1109–1112  
775 (2010).
- 776 75. Nikopoulos, K. *et al.* Next-Generation Sequencing of a 40 Mb Linkage Interval Reveals TSPAN12 Mutations  
777 in Patients with Familial Exudative Vitreoretinopathy. *The American Journal of Human Genetics* **86**, 240–  
778 247 (2010).
- 779 76. Ran, F. A. *et al.* Genome engineering using the CRISPR-Cas9 system. *Nature Protocols* **8**, 2281–2308  
780 (2013).
- 781 77. Schägger, H. Tricine–SDS-PAGE. *Nat Protoc* **1**, 16–22 (2006).
- 782 78. Wickham, H. *ggplot2: Elegant Graphics for Data Analysis*. (Springer-Verlag New York, 2016).
- 783
- 784